Development of Integrated SOL/Divertor Code and Simulation Study in JAEA

Hisato KAWASHIMA, Katsuhiro SHIMIZU, Tomonori TAKIZUKA, Shinji SAKURAI, Tomohide NAKANO, Nobuyuki ASAKURA and Takahisa OZEKI

Japan Atomic Energy Agency, Mukoyama, Naka 311-0193, Japan

(Received 12 December 2005 / Accepted 17 April 2006)

An integrated SOL/divertor code is being developed by the JAEA (Japan Atomic Energy Agency) for interpretation and prediction studies of the behavior of plasmas, neutrals, and impurities in the SOL/divertor region. A code system consists of the 2D fluid code for plasma (SOLDOR), the neutral Monte-Carlo code (NEUT2D), the impurity Monte-Carlo code (IMPMC), and the particle simulation code (PARASOL). The physical processes of neutrals and impurities are studied using the Monte Carlo (MC) code to accomplish highly accurate simulations. The so-called divertor code, SOLDOR/NEUT2D, has the following features: 1) a high-resolution oscillation-free scheme for solving fluid equations, 2) neutral transport calculation under the condition of fine meshes, 3) successful reduction of MC noise, and 4) optimization of the massive parallel computer. As a result, our code can obtain a steady state solution within 3 ~ 4 hours even in the first run of a series of simulations, allowing the performance of an effective parameter survey. The simulation reproduces the X-point MARFE (multifaceted asymmetric radiation from edge) in the JT-60U. It is found that the chemically sputtered carbon at the dome causes radiation peaking near the X-point. The performance of divertor pumping in the JT-60U is evaluated based on particle balances. In regard to the divertor design of the next tokamak of JT-60U, the simulation indicates the dependencies of pumping efficiency on the divertor geometry and operational conditions. The efficiency is determined by the balance between the incident and back-flow fluxes into and from the exhaust chamber.

Keywords: SOL/divertor code, simulation study, Monte Carlo method, JT-60U, X-point MARFE, divertor pumping, pumping efficiency

DOI: 10.1585/pfr.1.031

1. Introduction

In order to predict the controllability of particles and heat in the divertor of tokamak reactors such as the ITER [1] and to optimize the divertor design, a comprehensive simulation by the integrated modeling taking into account various physical processes is indispensable. For the design study of the ITER divertor, modeling codes such as B2 [2], UEDGE [3], and EDGE2D [4] have been developed, and their results have contributed to the evolution of the divertor concept.

In the Japan Atomic Energy Agency (JAEA), divertor codes have also been developed for the interpretation and prediction of the behaviors of plasmas, neutrals, and impurities in the SOL/divertor regions. We have been developing simulation codes originally, since physics models can be verified quickly and with flexibility under the circumstance of close collaboration with the JT-60 experimental team. Figure 1 shows our code system, which consists of the 2-dimensional fluid code SOLDOR [5], the neutral Monte Carlo code NEUT2D [5], and the impurity Monte Carlo code IMPMC [6]. The particle simulation code PARASOL [7] has also been developed in order to establish a physics modeling used in fluid simulations, such as the boundary condition at the divertor target and heat transport along the field line.

A combination of the SOLDOR and NEUT2D was

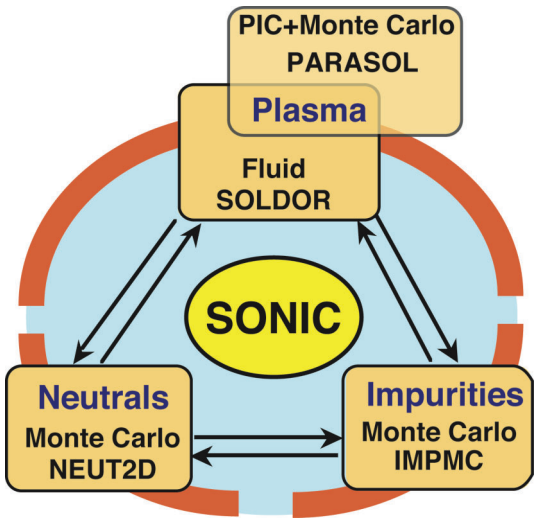

Fig. 1 Development of SOL/divertor codes and integration in the JAEA.

author's e-mail: kawashima.hisato@jaea.go.jp

completed. The features of this code are as follows: fine meshes near the divertor plates, complex divertor configurations including a pumping chamber, reduction of the Monte-Carlo noise in the neutral transport calculation, etc.

An integration of the SOLDOR, NEUT2D, and IMPMC codes is being carried out as a way to self-consistently simulate the SOL/divertor plasmas in the present tokamaks and in future devices. This integrated code is called the "SONIC" code.

In this paper, we describe the present status of SOL/divertor codes developed by the JAEA. A simulation study has been carried out for the JT-60U experiments [8,9] and for designing the divertor [10] of the next tokamak of JT-60U, National Centralized Tokamak (NCT)*), which is a modification program of the JT-60U to establish high beta steady-state operation [11]. We present the recent results of simulations of the X-point MARFE (multifaceted asymmetric radiation from edge) and divertor pumping in the JT-60U experiments. The particle controllability according to the divertor geometry (the width of exhaust slot) and the operational condition (the strike point position) is demonstrated for the NCT.

2. SOL/Divertor Codes in JAEA

In this section, the characteristics and present status of the SOL/divertor codes, SOLDOR, NEUT2D, IMPMC, and PARASOL, are presented.

2.1 SOLDOR code

The SOLDOR code is a 2D multi-fluid modeling for plasmas. The model equations are identical to the original B2-code [12], as follows:

$$\frac{\partial \rho_a}{\partial t} + \nabla\cdot\left(\rho_a v_{//a}\vec{b}\right) + \nabla\cdot\left(\rho_a \vec{v}_{\perp a}\right) = S_{\rho_a}\,, \tag{1}$$

$$\begin{aligned}&\frac{\partial}{\partial t}\left(\rho_a v_{//a}\right) + \nabla\cdot\left(\rho_a {v_{//a}}^2 + P_a\right)\vec{b} + \nabla\cdot\left(\rho_a v_{//a}\vec{v}_{\perp a}\right)\\ &+\left(\frac{Z_a n_a}{n_e}\right)\vec{b}\cdot\nabla\left(P_e\right) - P_a\,\nabla\cdot\vec{b}\\ &+\nabla\cdot\left(\vec{\Pi}_{//a}\right) = \sum_b R_{ab}^{\rm fric} + \vec{R}_a^{\nabla T}\cdot\vec{b} + S_{P_a//}\,,\end{aligned} \tag{2}$$

$$\begin{aligned}&\frac{\partial}{\partial t}\sum_a\left(\frac{3}{2}n_a T_i + \frac{1}{2}\rho_a v_{//a}^2\right)\\ &+\nabla\cdot\sum_a\left(\frac{3}{2}n_a T_i + \frac{1}{2}\rho_a v_{//a}^2 + P_a\right)v_{//a}\vec{b}\\ &+\nabla\cdot\sum_a\left(\frac{3}{2}n_a T_i + \frac{1}{2}\rho_a v_{//a}^2 + P_a\right)\vec{v}_{\perp a}\\ &+\nabla\cdot\sum_a\left(v_{//a}\vec{\Pi}_{//a}\right) + \nabla\cdot\sum_a\vec{q}_a\\ &= -v_{//e}\vec{b}\cdot\nabla P_e - n_e\nu_{eq}\left(T_i - T_e\right) + W_i\,,\end{aligned} \tag{3}$$

$$\begin{aligned}&\frac{\partial}{\partial t}\left(\frac{3}{2}n_e T_e\right) + \nabla\cdot\left(\frac{3}{2}n_e T_e + P_e\right)v_{//e}\vec{b}\\ &+\nabla\cdot\left(\frac{3}{2}n_e T_e + P_e\right)\vec{v}_{\perp e} + \nabla\cdot\vec{q}_e\\ &= +v_{//e}\vec{b}\cdot\nabla P_e + n_e\nu_{eq}\left(T_i - T_e\right) + W_e\,,\end{aligned} \tag{4}$$

where the suffix of "a" denotes the ion species, $\vec{b}$ is the unit vector along the magnetic field line, $\rho_a = m_a n_a$ is mass density, $v_{//a}$ is parallel velocity, $v_{\perp a} = -D_{\perp a}/n_a\cdot\nabla_\perp n_a$ is cross field anomalous velocity, T_i is ion temperature, and T_e is electron temperature. The viscosity term $\vec{\Pi}_{//a} = -\eta_{//a}\nabla_{//}v_{//a} - \eta_{\perp a}\nabla_\perp v_{//a}$, the ion and electron heat conduction $\vec{q}_{i/e} = -\kappa_{i/e}^{//}\nabla_{//}T_{i/e} - \kappa_{i/e}^{\perp}\nabla_\perp T_{i/e}$, the equi-partition $n_e\nu_{eq}(T_i - T_e)$, the friction force with b-species $R_{ab}^{\rm fric}$, and the thermal force $\vec{R}_a^{\nabla T}$ are included in the model equations. The term $\vec{b}\cdot\nabla P_a$ in the momentum equation is converted into $\vec{b}\cdot\nabla P_a = \nabla\cdot(\vec{b}P_a) - P_a\nabla\cdot\vec{b}$, and the term $v_{//e}\vec{b}\cdot\nabla P_e$ in the energy equations represents the energy related to the electric field. The transport along the field line is assumed to be classical. The boundary condition at the divertor plates is as follows:

$$v_{//i} = C_s \equiv \left(\frac{T_i + T_e}{m_i}\right)^{1/2}, \tag{5}$$

$$Q_i = \gamma_i T_i n_i v_{//i} + \frac{1}{2}m_i v_{//i}^2 n_i v_{//i}\,, \tag{6}$$

$$Q_e = \gamma_e T_e n_e v_{//e}\,, \tag{7}$$

where Q_i, Q_e are the parallel heat flux densities and γ_i, γ_e are the heat transmission factors ($\gamma_i = 2.5$ and $\gamma_e = 4.0$ [12]). These conditions will be improved to the accurate ones on the basis of the PARASOL simulation results, as discussed in Sec. 2.4.

The diffusion coefficients across the field, such as $D_{\perp a}$, $\eta_{\perp a}$, $\kappa_i^\perp = n_i\chi_i^\perp$, $\kappa_e^\perp = n_e\chi_e^\perp$, are assumed to be anomalous and spatially constant. The terms of the right-hand side, S_{ρ_a}, $S_{p_{a//}}$, are sources of mass and the momentum of a-species, while W_i, W_e are sources of ion and electron energy, respectively. These source terms arise from the interactions with neutral particles. Therefore, the plasma transport and the neutral transport must be solved consistently.

In order to solve the system of the above equations, we must address five difficult requirements. Here we briefly describe our measures to solve these problems as features of the SOLDOR code.

**** Complex divertor structure***

The finite volume method (FVM) is adopted for discretization in space. The boundary-fitted grid is applied near the divertor plates while the orthogonal grid is applied in the SOL and the core. Fine meshes (≤ 2 mm) are used around the divertor target as shown in Fig. 2. This mesh size is remarkably fine compared with the size of the meshes near targets in the conventional code, typically on the order of $\sim$ cm.

*) The JT-60U modification is renamed from NCT to JT-60SA (Super Advanced) at present.

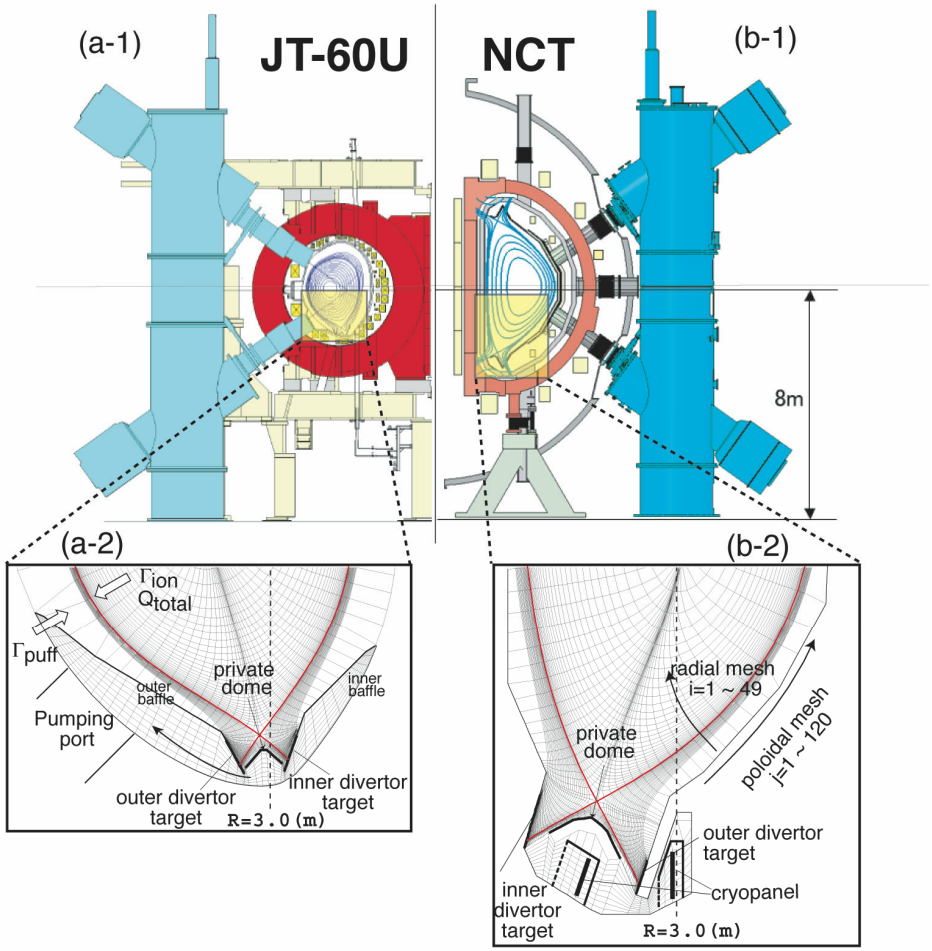

Fig. 2 (a-1), (b-1) ; the schematic cross sections of the JT-60U and the NCT. (a-2), (b-2) ; their mesh structures for the SOLDOR/NEUT2D simulations.

**** Strong nonlinearity of equations***

Non-linear equations are linearized by the Newton-Raphson method in order that physical terms can be easily included or modified to extend the code. Not only the steady state solution but also the time evolution of the plasma parameters can be investigated using this code.

**** Two-dimensional problem***

The finite difference equations are solved using the approximate factorization (AF) method, where a two-dimensional system is split into two one-dimensional systems in the poloidal and radial directions. The AF method obtains the solution in two steps at every time step. The equations in each step can be solved efficiently, because they are a block tridiagonal system. The code can be extended to three dimensions straightforwardly.

**** Numerical stability for convective terms***

Numerical treatment of the convective terms, such as $\nabla\cdot\left(\rho_a v_{//a}\vec{b}\right)$, $\nabla\cdot\left(\rho_a v_{//a}^2 + P_a\right)\vec{b}$, is generally very difficult to perform. An inadequate scheme results in a solution containing numerical oscillation. We apply the total variation-diminishing (TVD) scheme [13] for the convective terms. This scheme adds the minimum dissipation according to need as a method to obtain a solution without numerical oscillation. It can simulate even a shock wave without deforming the shock front. Therefore, the TVD scheme is the most familiar one in computational fluid dynamics.

**** Couple with Monte-Carlo code***

In some divertor codes, the fluid equation is used for the neutral transport as well as for plasma ions. However, the neutral transport must be solved using a Monte-Carlo code in order to analyze the experimental data in detail or to perform a design study. The MC calculation requires a relatively large amount of computational time and its result contains a degree of MC noise, which deteriorates the convergence toward a steady state solution. This matter is described in Sec. 2.2.

The code is formulated for multi-ion plasma, but impurity ion transport is not treated in the current version. In the near future, impurity transport is consistently solved using the impurity Monte-Carlo code, IMPMC, as dis-

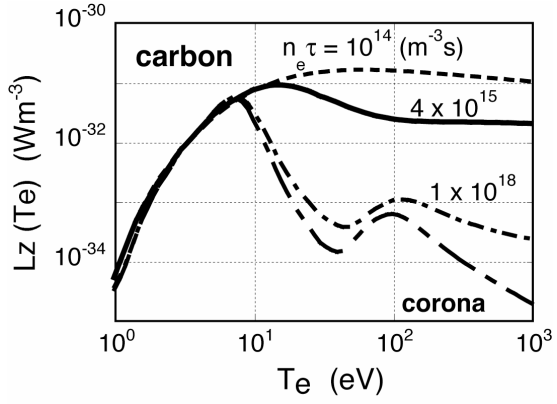

Fig. 3 Carbon radiation coefficient for the simplified non-corona model.

Table 1 Collision processes between neutral and plasma particles in the NEUT2D code.

atom	I_e	e + D	→	e + D^+ + e
	CX	D^+ + D	→	D + D^+
	EL_a	D^+ + D	→	D^+ + D
molecular	I_e	e + D_2	→	e + D_2^+ + e
	DS	e + D_2	→	e + D + D
	DS	e + D_2	→	e + D^+ + D + e
	EL_m	D^+ + D_2	→	D^+ + D_2
ion	DS	e + D_2^+	→	e + D^+ + D
	DS	e + D_2^+	→	e + D^+ + D^+ + e
	DS	e + D_2^+	→	D + D
	RC	e + D^+	→	D

cussed later in Sec. 2.3. A simple radiation model is employed in which a fraction of carbon impurity is assumed to be a fixed value, typically 1∼2% of the deuterium density, and the radiation loss is evaluated by $W_r = -n_e n_z L_z(T_e)$. The radiation loss rate $L_z(T_e)$ is enhanced by the impurity recycling effect, assuming $n_e\tau_{recycle} = 4 \times 10^{15}$s m^{-3} [14], as shown in Fig. 3.

2.2 NEUT2D code

The NEUT2D code calculates the neutral density (n_0) and the source terms (S_{ρ_a}, $S_{p_{a//}}$, W_i, W_e). We explain the Monte-Carlo techniques used in the code as an example of tracking a D atom. The neutral particles move at a constant velocity until a collisions takes place. The collision point is determined from the relation of

$$\int_0^L \mathrm{d}s/\lambda_{tot}(s) = -\ln\xi, \tag{8}$$

where L is the free flight length, $\lambda_{tot}(s)$ the local mean free path, s the distance from the previous collision point along a straight line, and ξ a uniform random number. The local mean free path of atom $\lambda_{tot}(s)$ is summed over ionization by electrons (I-e), charge exchange (CX), and elastic collisions (EL_a) as follows:

$$1/\lambda_{tot}(s) = 1/\lambda_{ion} + 1/\lambda_{CX} + 1/\lambda_{EL\_a}. \tag{9}$$

When a collision occurs, the collision type, CX or EL_a, is chosen in accordance with its probability. The weight, corresponding to test flight neutral flux, is reduced by ionization [15];

$$w_{new} = w_{old} \cdot \frac{1/\lambda_{CX} + 1/\lambda_{EL\_a}}{1/\lambda_{ion} + 1/\lambda_{CX} + 1/\lambda_{EL\_a}}. \tag{10}$$

This technique, called "suppression of absorption", effectively reduces the variance. The tracking of a test particle is continued after selecting a new velocity according to either a CX or EL_a collision. The track-length estimator method is used as the scoring method to calculate the neutral density and source terms. Neutral moleculues are also traced with the same technique. The collision between neutral and plasma particles included in the NEUT2D code is listed in Table 1. As for the molecular ions D_2^+, a dissociation process is assumed to occur immediately after an ionization event in a molecule. The mean free path of this dissociation process in the poloidal plane is less than 1 mm and can be neglected.

The features of the NEUT2D code are as follows.

**** Region to trace neutral particle***

To accurately evaluate the particle balance in the system, the neutral particle transport is solved inside the whole vessel: the core region ($r/a \leq 1.0$), the SOL/divertor, and the vacuum region including the exhaust structure. In other divertor codes, generally the neutral particles are assumed to be absorbed at the core edge and the complicated structure of the exhaust system is simplified.

**** Fine mesh near divertor plates***

Figure 4 shows a typical variation of neutral density along the poloidal direction in JT-60U simulations. The characteristic length L_c changes from ∼2 mm in attached plasma to ∼2 cm in detached plasma. The mesh size near the plates must be around 2 mm as shown in Fig. 2 in order to simulate the transition between attached and detached conditions. The reduction of mesh size below 1 cm was generally difficult since the MC noise increased significantly with a decrease of the mesh size.

**** MC noise reduction***

We have succeeded in reducing the MC noise by introducing a newly developed "piling" method (averaging the Monte Carlo result in time) [as described in the appendix]. This method enables us to use the fine mesh.

**** Particle balance***

Monte-Carlo calculations are performed for the neutral particles recycled at the outer target, the inner target, the wall facing the SOL or the wall in the private region, and the volume source due to recombination and gas puff. These 6 source terms are renormalized by each neutral flux

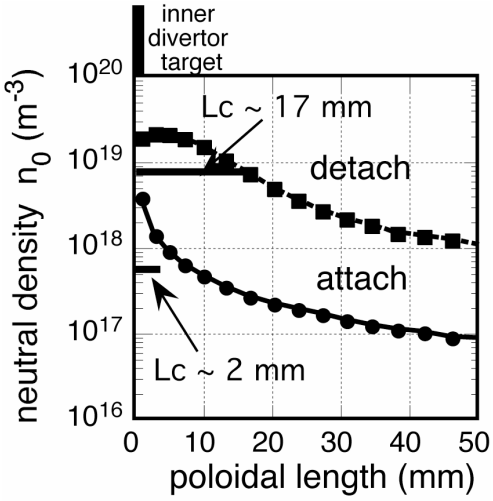

Fig. 4 Neutral density profiles along the poloidal length from the inner divertor target at attached and detached plasmas. The spatial resolutions of the calculation need to be below the characteristic length $L_c = n_0(dn_0/dr)^{-1}$ of ~2 mm.

in each iteration step of the SOLDOR code (refer to the use of the Newton-Raphson method). Convergence to steady state is assured by this careful treatment of the particle balance between the SOLDOR and NEUT2D codes.

**** Optimization on parallel computer***

We have optimized the NEUT2D code performance by using Message Passing Interface (MPI) on the massive parallel computer, SGI ALTIX 3900. As a result, a steady state solution can be obtained within a short computational time of 3~4 hours even in the first run of a series of simulation studies, which is about 10 times faster than the conventional divertor codes coupled with the MC code. Thus our code enables effective parameter survey.

The SOLDOR and NEUT2D codes have been successfully combined and used in experimental analysis and divertor design. We adopt a model that calculates energy and momentum source terms arising from the atomic and molecular reactions in the DEGAS code [16]. The plasma boundary in SOLDOR is set at $r/a = 0.95$. The profiles for $n_e(r), T_e(r)$ and $T_i(r)$ in $r/a < 0.95$ in the NEUT2D calculations are specified with each function. For example, the density profile has a function of $n_e(r) = (n_{e0} - n_{eb}) \cdot \left\{1 - (r/0.95a)^2\right\}^m + n_{eb}$, where n_{eb} is the density at the boundary ($r/a = 0.95$) calculated in the SOLDOR, and m is fixed at 0.3 ~ 0.5. Total power and particle fluxes (Q_{total}, Γ_{ion}) across the $r/a = 0.95$ surface are given as the input parameters. The recycling of deuterium is assumed to be 100% at the first wall. The treatment of the interaction with walls is the same as that in the DEGAS code. The pumping speed is specified by an albedo for neutrals in front of the exhaust port or cryopanel. Under these conditions, the neutral transport and the plasma transport in the divertor/SOL region including the core edge ($r/a \geq 0.95$) are simulated self-consistently.

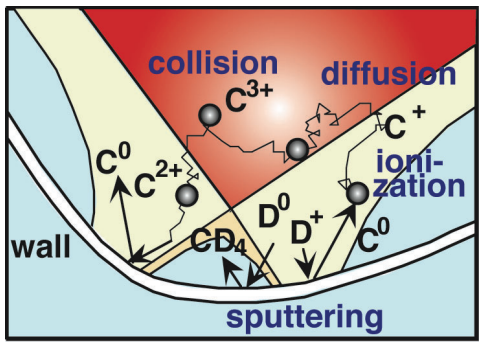

Fig. 5 Illustrations of various processes treated in the IMPMC code.

2.3 IMPMC code

Simulation codes for impurity transport are classified basically into fluid codes and Monte Carlo codes. In most 2D multi-fluid divertor codes [2–4], impurity transport is solved simultaneously as a fluid species. On the other hand, some elaborate Monte Carlo codes have been developed for the interpretation of impurity behavior in the divertor, e.g., DIVIMP [17] and IMPMC [6]. In these Monte Carlo codes, impurity transport is solved under the background plasma parameters obtained by a simple divertor code named the "Onion-Skin model" [18], in order to take full advantage of the available experimental data.

We regard the Monte Carlo modeling for impurity transport as superior to fluid modeling in regard to kinetic effects and the modeling of impurity generation and interactions between impurities and walls. The neglect of the thermalization process for impurity ions, i.e., an assumption of $T_{imp} = T_i$ used in fluid model, is actually invalid for impurities with low charge states near the divertor plates [19]. The kinetic effects alter the thermal force. The direction of the thermal force on impurity ions having a high velocity (the order of thermal velocity of plasma ions) is opposite that of the fluid approximation [20, 21]. The dissociation processes of methane, which are very complicated [22, 23], are impossible to treat using fluid modeling.

For impurity transport, therefore, the IMPMC code has been developed based on Monte Carlo techniques [24]. This model includes (1) impurity generation due to physical and chemical sputtering, (2) ionization of sputtered neutrals and the dissociation processes of methane, (3) parallel motion of impurity ions along field lines, (4) Coulomb scattering, (5) cross-field diffusion, and (6) atomic processes (ionization and recombination), as shown in Fig. 5.

The features of the IMPMC code are as follows.

- Impurity transport is simulated in realistic divertor geometry; accordingly, comparison with experimental data can be accomplished in detail.
- Impurity outfluxes due to physical sputtering, self-sputtering, and chemical sputtering are determined self-consistently.

- Diffusion processes in velocity space for Coulomb scattering are simulated using a Monte Carlo method, simultaneously taking into consideration the parallel motion of impurity ions.
- The dynamics of methane (CD_4) are simulated. Methane is generated by chemical sputtering on the assumption of the yield $Y_{CD_4} = 0.05$ [25]. All the dissociation processes (CD_3^+, CD_3, CD_2^+, etc) are included in the MC modeling.

Detailed modeling for methane proved that hydrocarbons chemically sputtered from the private wall by neutral particles plays important roles in carbon contamination near the X-point in high density divertor plasma [23, 26].

A conventional MC algorithm for the diffusion process in velocity space has a disadvantage in that the impurity ions must be traced with a time step shorter than the slowing down time ($\Delta t \ll \tau_s$). The first version of IMPMC code demands a huge amount of computational time in the case of detached plasma because of this extremely short slowing down time, typically, $\tau_s \sim 4 \times 10^{-9}$ s for C^{3+}. Thus, we have developed a new diffusion model to resolve this defect in the Monte-Carlo code.

The impurity ions are diffused in the velocity space by Coulomb collisions with the plasma ions, resulting in diffusion along the magnetic field line in real space. The IMPMC code correctly treats the velocity-space diffusion (VD model) for this process. The DIVIMP code has previously employed the spatial diffusion model (SD model), where this process was simulated by adding random displacement of $\Delta s = \sqrt{2D_{//}\Delta t} \cdot r_G$ at every step. Here, s is the parallel position, $D_{//} = v_{th}^2 \tau_s$ is the parallel diffusion coefficient, and r_G is the normal random number. Comparing these two models, we pointed out that the SD model cannot be applied for plasma in which the characteristic time of parallel motion is comparable to collision time [27]. The SD model in the DIVIMP code was replaced with the VD model at need [28].

We have reformulated these processes, i.e., the relation between the velocity and spatial diffusion processes. These processes are described by the Langevin equations,

$$\begin{aligned} s^{n+1} &= s^n + v_{//}^n \Delta t \,, \\ v_{//}^{n+1} &= v_{//}^n - (v_{//}^n - V_f)\Delta t/\tau_s \\ &\quad + F_{//}\Delta t/m_z + \{< \Delta v_{//}^2 > \Delta t\}^{1/2} r_G, \end{aligned} \tag{11}$$

where the index n is the time step number, $< \Delta v_{//}^2 > \Delta t$ is the mean square deviation of parallel velocity change during a time step Δt, and V_f is the plasma flow velocity. We are developing a new algorithm to simulate this parallel diffusion process with a time step much larger than τ_s. Details of the new diffusion model will be published elsewhere [29]. The means and the standard deviations of the parallel position s and the parallel velocity $v_{//}$ in the simulation obtained by the VD model are denoted by symbols in Fig. 6. We used the parameters of $s(t=0) = 0, v_{//}(t=0) = 2$, $V_f = 0$, $F_{//} = 0$, $\langle \Delta v_{//}^2 \rangle \Delta t = 0.025$, $\tau_s = 0.2$, $\Delta t = 0.01$, and N (number of test particles) = 5000. Results of model simulations (symbols) agree well with analytical solutions of Langevin equations (solid lines). Then the position of the test particle at any time can be chosen from the normal distribution with mean $\langle s \rangle$ and standard deviation σ_S^2 obtained from the analytical solution. The parallel velocity is also chosen from the normal distribution with mean $\langle v \rangle$ and standard deviation σ_v^2. This model neglects the correlation between space and velocity in the early phase ($t \ll \tau_s$). It should be noted that the distribution at any time, not only $t \gg \tau_s$ but also $t \leq \tau_s$, can be determined as far as impurity ions stay in the region where the plasma parameters are considered to be nearly constant. In the case where the parallel transit time is comparable to the slowing down time, i.e., attached plasma, the VD model should be employed for this diffusion process.

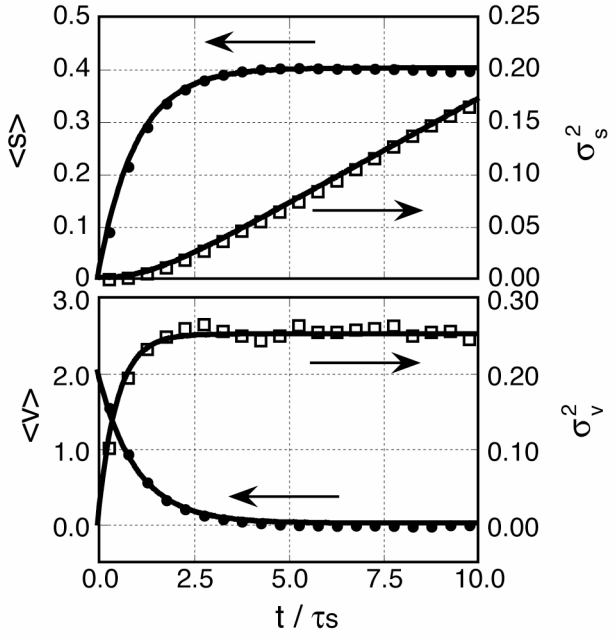

Fig. 6 The means and the standard deviations (σ^2) of the parallel position (s) and the parallel velocity ($v_{//}$) in the new diffusion model (solid line) and the VD model (symbols).

The cpu time can be significantly reduced by this new algorithm. In a case where 5000 test particles were traced during 1 msec in the typical detached divertor plasma ($n_e \sim 1 \times 10^{20}$ m^{-3}, $T_e \sim 1$ eV, see Fig. 8), the conventional method ($\Delta t = (1/20)\tau_s$) took 1 hour whereas new algorithm ($\Delta t = 10^{-6}$ s) took only 12 sec.

Using the new diffusion model, we have obtained a prospect of the self-consistent modeling of divertor plasmas and impurity transport, combining the SOLDOR/NEUT2D and the IMPMC codes. This unified code, named SONIC [29], will clarify the impurity transport in consideration of kinetic effects and chemically sputtered carbon.

2.4 PARASOL code

Analyses of divertor experiments in present devices and predictions of divertor performance in future reactors have been carried out by using comprehensive simulation codes with the fluid model, such as the B2, UEDGE, EDGE2D, and SOLDOR codes. In the fluid model for SOL/divertor plasmas, however, various physics models are introduced, i.e., boundary conditions at the plasma-wall boundary, heat conductivity, viscosity and so on. A kinetic approach is required to examine the validity of such physics models, and to improve/develop accurate physics models. One of the most powerful kinetic models is particle simulation. In order to satisfy the above-mentioned requirement, we have been developing a particle simulation code called PARASOL (PARticle Advanced simulation for SOL and divertor plasmas). There are various versions of the PARASOL code: 1D (one-dimensional) PARASOL, 2D (two-dimensional) slab PARASOL, 2D separatrix PARASOL, etc. Details of the simulation model of PARASOL have been described in Ref. 7. Figure 7 shows a frame sketch of the PARASOL code. The outline of each part is briefly presented below.

This model is fundamentally a time-dependent electrostatic particle-in-cell (PIC) model. The electrostatic potential, including the sheath potential at the plasma-wall boundary, is self-consistently calculated using Poisson's equation. Although the system size L is very much larger than the Debye length λ_D in real plasmas, PARASOL simulations with the grid size Δ of the order of λ_D are available to study such plasmas with smaller values of $L/\lambda_D = 10^2 \sim 10^3$. This is because the characteristics of SOL/divertor plasmas are almost unchanged by changing L/λ_D except for the sheath region. The simulation domain is bounded by walls. A magnetic configuration is given and part of (or all) field lines intersects the walls. The 1D PARASOL system is bounded by two divertor plates, while the 2D PARASOL system is surrounded by walls. This system treats charged particles and neutral particles. Ion orbits are fully traced in this given magnetic field and the electrostatic field is calculated self-consistently, while guiding-center orbits are followed for electrons.

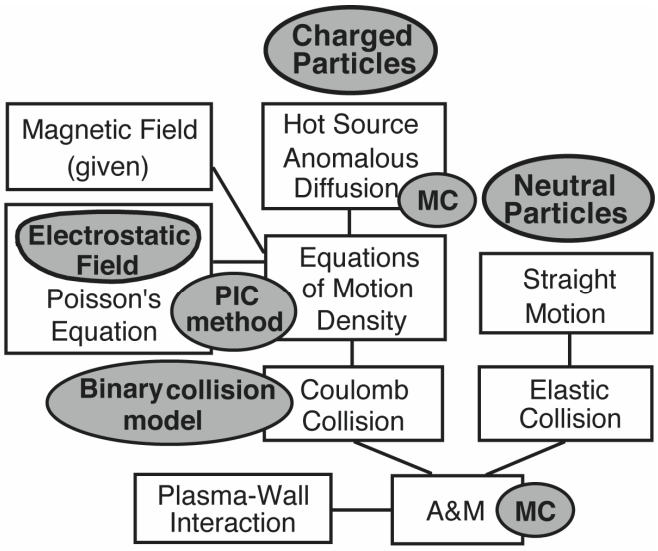

Fig. 7 Frame sketch of the PARASOL code.

The effect of drift in SOL/divertor plasmas is fully simulated by the PARASOL code. The full-orbit calculation provides a complete description of the ion polarization drift, which is essential for magnetic pre-sheath formation in the magnetic field intersecting a divertor plate obliquely [30, 31]. The $E \times B$ drift influences the SOL flow speed as well as the flow speed at the plasma-wall boundary [31, 32]. The $E \times B$ drift in the magnetic pre-sheath is a key factor for 2D sheath formation, which has not been considered in fluid simulations. Analytic forms of the boundary conditions applicable to the fluid code have been established on the basis of PARASOL simulations. These new conditions, instead of the simple ones described in Sec. 2.1, will be incorporated into the SOLDOR code after the code is improved to treat drift flows.

Anomalous transport across the magnetic field lines is simulated using a Monte Carlo technique. A spatial displacement perpendicular to the magnetic field is added randomly for every time step after the ordinary motion.

The deformation of the velocity distribution function from the Maxwellian affects the sheath characteristics. This deformation is essential for the heat transport parallel to the magnetic field line in SOL/divertor plasmas. Coulomb collisions, therefore, play a very important role in SOL/divertor plasmas. The collisional diffusion in the velocity space is the main mechanism to supply high-energy electrons. These electrons can escape to the divertor plate, while low energy electrons are trapped in a SOL plasma by the sheath potential. The PARASOL code employs a Monte-Carlo binary collision model [33]. At every time step a particle in a cell suffers binary Coulomb collisions with an ion and an electron, which are chosen randomly in the same cell. The change in the relative velocity due to binary collisions is added after computing the collisionless motion. Total momentum and total energy are conserved intrinsically.

The heat transport parallel to the magnetic field is dependent on the collisionality, and the ratio of the system size to the mean free path. In high-collisional plasmas, transport is the classical conduction. In low-collisional plasmas, transport is the free-motion flux. The quantitative evaluation and approximate expression were obtained using 1D PARASOL simulations [7]. Transient properties of the transport after an ELM crash have been recently studied. It was found that kinetic effects on this transient transport are very important compared to those on stationary transport [34, 35]. These transport coefficients affected by kinetic effects will be incorporated into the SOLDOR code.

The PARASOL code can simulate behaviors of neu-

tral particles simultaneously with those of charged particles. We optionally simulate the effects of neutrals on the basis of simplified models instead of treating neutral particles directly. The characteristic length L_{AM} related to atomic and molecular processes is usually much smaller than the whole system size L. When we study the physics including such shorter characteristic length, we set the PARASOL system carefully so that $L \gg L_{AM} \gg \Delta$. It is not necessary to set these values as the same as those of realistic SOL/divertor plasmas. The purpose of PARASOL simulation is to study the basic physics.

Plasma control methods are easily introduced into PARASOL simulations. Divertor biasing is simply given by the wall boundary condition in Poisson's equation. The effects of biasing on the SOL flow were investigated using 2D PARASOL simulation. The asymmetry of the SOL flow can be controlled by the biasing [32].

Thus, establishment of physics modeling in the PARASOL code is progressing. Through the development of our code system described in Fig. 1, we aim to verify the physics models used in the fluid code SOLDOR on the basis of the PARASOL simulation.

3. Recent Simulation Results

Efforts towards the integration of the SOLDOR, NEUT2D, and IMPMC codes are being made. The SOLDOR and NEUT2D codes have been successfully combined and improved to speedily obtain a steady state solution as a result of the success in the reduction of MC noise and optimization on the parallel computer. The IMPMC code has been improved, i.e., the calculation efficiency in the detached plasma has been significantly increased with the new diffusion model. Simulations using these codes have been performed for analyses of the JT-60U divertor experiments and for study of the NCT divertor design.

3.1 Analysis of X-point MARFE in the JT-60U

Detached divertor by strong gas puffing has been studied as a way to reduce the heat load on the divertor target. However, in discharges with such divertor plasmas, radiation near the X-point is enhanced locally and often leads to a MARFE (multifaceted asymmetric radiation from edge). The main plasma is cooled directly due to the deterioration of the impurity shielding effect, and the energy confinement is then degraded. In order to understand the physical process in a MARFE, JT-60U detached divertor plasmas with X-point MARFE are simulated using the SOLDOR/NEUT2D code with employing the simplified non-corona radiation model. The simulation is carried out for the JT-60U at an equilibrium of I_p/B_T= 1.5 MA/3.0 T in the lower single null divertor configuration. The total power flux Q_{total} = 2 MW and the particle outflux of $\Gamma_{ion} = 0.2 \times 10^{22}\,s^{-1}$ are used under the experimental conditions. We assume a particle diffusion coefficient $D_\perp = 0.3\,m^2/s$ and a thermal diffusivity of electron and ion $\chi^e_\perp = \chi^i_\perp = 1\,m^2/s$. Those transport coefficients have been chosen based on the evaluations of various tokamaks [36]. The convective transport perpendicular to the magnetic field is not taken into account at present. The recycling coefficients at the divertor plates and walls are set to 1.0 for ion and neutral particles. The fraction of carbon impurity to ion density is assumed to be 1%.

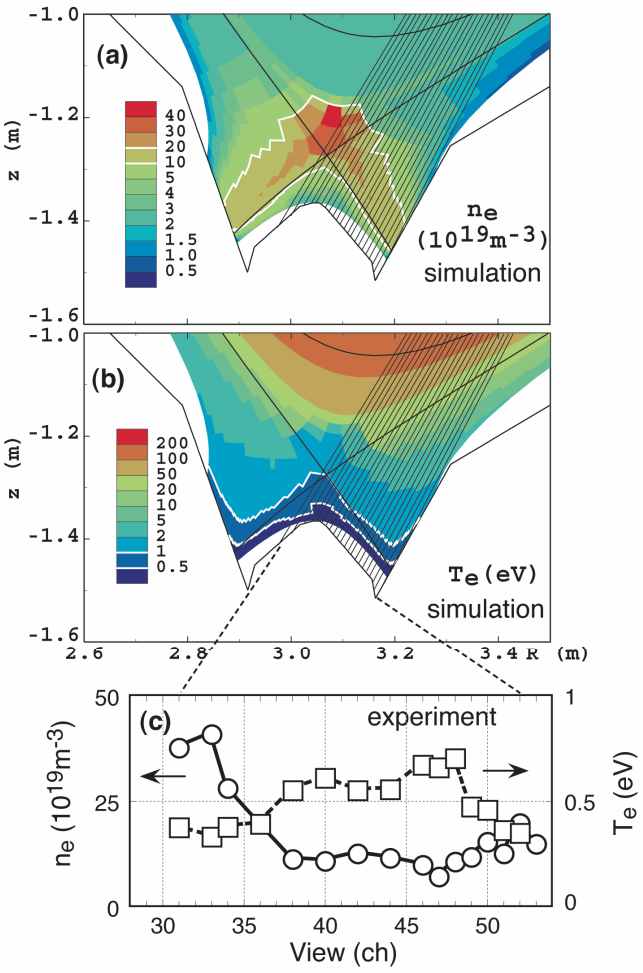

Fig. 8 Contour plots of the calculated electron density (a) and temperature (b) in the divertor region at a simulation of the JT-60U X-point MARFE by the SOLDOR/NEUT2D code. The regions of n_e=10-20 ($10^{19}m^{-3}$) and of T_e=0.5-1 (eV) are bounded by white lines. (c) Density and temperature profiles obtained by the spectroscopic measurement along the viewing lines (set of solid lines in (a) and (b)).

Figures 8 (a) and (b) show the contour plots of the calculated electron density and temperature. The X-point MARFE with peaked density $n_e \sim 4 \times 10^{20}\ m^{-3}$ arises with introducing the strong gas puffing of $0.8 \times 10^{22}\,s^{-1}$. Electron temperature is in the range of 0.5 ~ 1 eV from the divertor target to the X-point along the separatrix. This is in contrast to that in the attached plasma (from 10 eV to 100 eV). Figure 8 (c) shows the density and temperature

profiles obtained by the spectroscopic measurement along the viewing lines (solid lines in Figs. 8 (a) and (b)) for the JT-60U experiment [37]. The measurement is carried out using the Stark broadening and assuming the Boltzmann distribution in the volume recombination plasmas [38]. Approaching the X-point, the density further increases up to $4 \times 10^{20}\mathrm{m}^{-3}$ and the electron temperature decreases to $0.5 \sim 1$ eV. It is found that the calculated density and temperature profiles fairly agree with those of the experiment.

The characteristics of the X-point MARFE can be qualitatively reproduced by the present code. In order to study the quantitative characteristics, further simulation analyses will be carried out using the integrated SONIC code, which contains the elaborated Monte Carlo impurity code.

In regard to radiation, the bolometer measurement indicated that the peaked value reached several $\mathrm{MW/m^3}$ [39]. Using the plasma profile calculated as shown in Fig. 8, the impurity transport is investigated using the IMPMC code. This code includes the modeling of the dissociation process of methane and the dynamics of dissociation products (CD_3^+, CD_3, CD_2^+, etc). For simplicity, these complicated dissociation processes of CD_4 are not taken into account in the present calculations. Instead, we treat chemically sputtered CD_4 as a carbon C with a low energy (~1 eV). Figure 9 shows the ionization points of carbon chemically sputtered from the divertor targets and the dome under attached and detached conditions, respectively. The chemical sputtering yield is set to $Y_{CD_4} = 0.05$. For the attached case, the carbon is ionized near the divertor target and most ions return to the target due to the friction force. In contrast, the carbon atom can penetrate the X-point for the detached case as shown in Fig. 9. After the pre-calculation of the ionization process, the IMPMC simulation is performed in which the transport and atomic processes including the charge exchange recombination are traced. The radiation power near the X-point reaches $3\sim4\,\mathrm{MW/m^3}$, which is consistent with the experimental result. It is found that the radiation is brought dominantly by the deep penetration of neutral carbons sputtered from the private dome and the divertor targets. This outflux of carbon in the simulation corresponds to that of methane chemically sputtered by neutral particles.

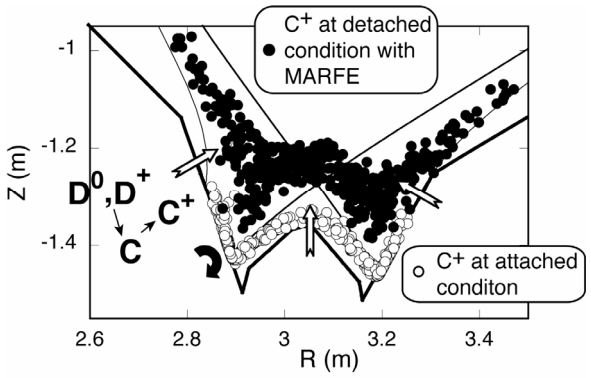

Fig. 9 Simulations of carbon impurity transport at attached condition (open circle) and detached condition with the X-point MARFE (closed circle) by the IMPMC code.

Thus, a high accuracy analysis of the X-point MARFE is performed using the divertor code, taking advantage of the fine mesh and MC modeling.

3.2 Simulation of divertor pumping in the JT-60U

Divertor pumping is a key issue for particle control in the steady state high beta operation of future tokamak devices. In order to extrapolate the divertor pumping characteristics from the present experimental data, a simulation of divertor pumping in the JT-60U is carried out using the SOLDOR/NEUT2D code, whose results are compared with the experimental results [40].

To investigate the effect of the equilibrium configuration on divertor pumping, the strike positions were changed in the simulations as shown in Fig. 10. The parameters of $I_p/B_T = 1.5\,\mathrm{MA}/3.5\,\mathrm{T}$, $Q_{total} = 5 \sim 7\,\mathrm{MW}$, $\Gamma_{ion} = 0.1\times10^{22}\,\mathrm{s}^{-1}$, $D_\perp = 0.3\,\mathrm{m^2/s}$, and $\chi_\perp^e = \chi_\perp^i = 1\,\mathrm{m^2/s}$ are used under the experimental conditions with NBI heating. With these fluxes and diffusion coefficients, the simu-

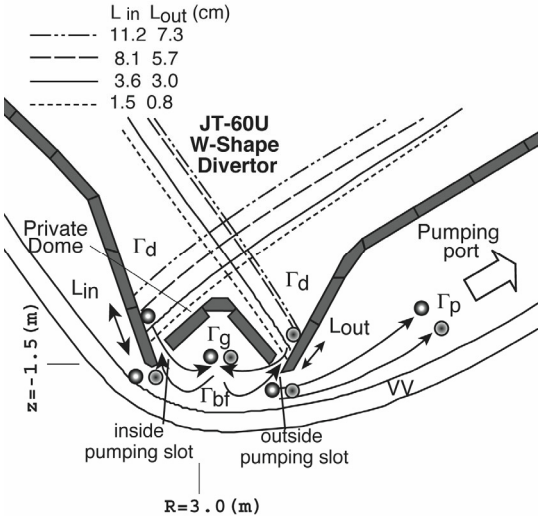

Fig. 10 Illustration of the strike point scan for the simulation of divertor pumping in JT-60U by the SOLDOR/NEUT2D code. The position is defined by (L_{in}, L_{out}), the distance from the private dome wing extension point on the target to the strike point of separatrix. Motions of neutral flows associated with the fluxes (Γ_d, Γ_g, Γ_{bf} and Γ_p) are also illustrated for interpretation of the simulation results. Γ_d is the generated flux on the divertor target, Γ_g is the flux into the exhaust chamber through the slot, Γ_{bf} is the backflow flux from the exhaust chamber to the plasma side, and Γ_p is the pumping flux, respectively. Note $\Gamma_p = \Gamma_g - \Gamma_{bf}$ in the steady state.

lation reproduces the experimental divertor plasmas fairly well. The fraction of carbon impurity to ion density is assumed to be 2%. The pumping is performed using only the inside pumping (IP) slot and both-side pumping (BP) slots with a fixed pumping speed $S_{\rm pump} = 40\,{\rm m}^3/{\rm s}$ in front of the pumping port. The exhaust chamber through below the private dome to the outer pumping port is not changed for both cases; namely, it is not divided into an inner and an outer side even in the BP case. The neutral fluxes around the divertor are analyzed to clarify the pumping characteristics. The fluxes are classified as $\Gamma_{\rm d}$ (the generated flux at the divertor targets), $\Gamma_{\rm g}$ (the flux into the exhaust chamber through the slot), $\Gamma_{\rm bf}$ (the back-flow flux from the exhaust chamber to the plasma side), and $\Gamma_{\rm p}$ (the pumping flux), as shown in Fig. 10. The pumping efficiency $\eta_{\rm p}$ [$\equiv \Gamma_{\rm p}/\Gamma_{\rm d}$] is compared among those conditions. In both attached cases, the gas puff flux $\Gamma_{\rm puff}$ is fixed to 1×10^{21} m^3/s. In the both MARFE cases, it is changed to $8 \sim 25\times10^{21}$ m^3/s along the experiments because the MARFE generation is restricted depending on the strike point position and the gas puff flux. The results in Fig. 11 (a) show that 1) $\eta_{\rm p}$ decreases with an increase of ($L_{\rm in}$, $L_{\rm out}$), 2) $\eta_{\rm p}$ at IP becomes larger than that at BP within a factor of three, and 3) $\eta_{\rm p}$ is enlarged remarkably under the MARFE conditions. Comparison of $\Gamma_{\rm p}$ with measurement and simulation at $L_{\rm in} \sim L_{\rm out} \sim 3$ cm is shown in Fig. 11 (b). The $\Gamma_{\rm puff}$ in the simulation is adjusted to that in the measurement data. These values show fairly close agreement together with the above dependencies on IP, BP, and the attached and detached conditions.

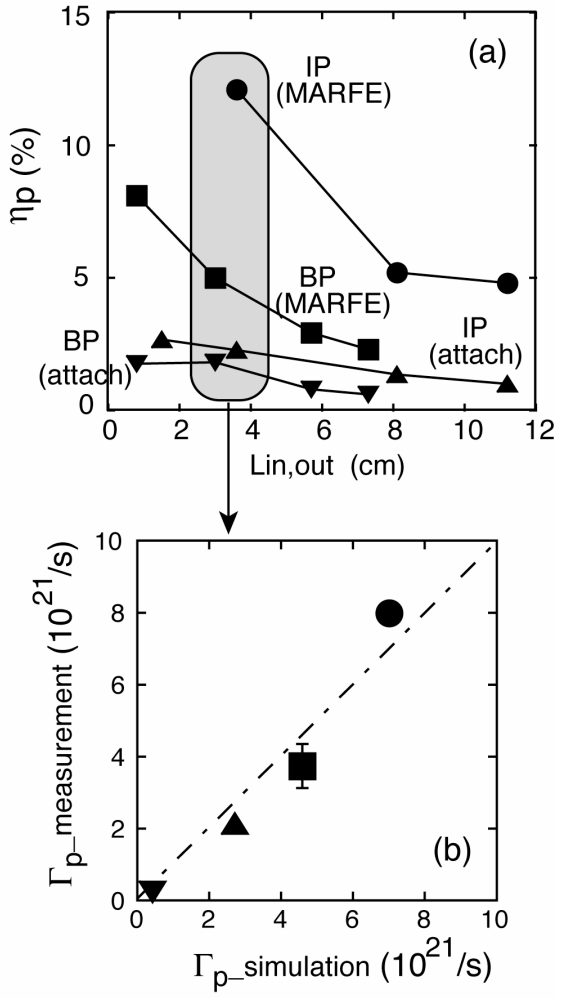

Fig. 11 (a) Pumping efficiency $\eta_{\rm p}$ ($\equiv \Gamma_{\rm p}$ / $\Gamma_{\rm d}$) obtained by the simulations as a function of $L_{\rm in}$ for IP (inside pumping) and of $L_{\rm out}$ for BP (both-side pumping) based on the experiments. Symbols correspond to the cases of IP with MARFE (●), BP with MARFE (■), and IP (▲) and BP (▼)at attached conditions. (b) Comparisons of the pumping flux $\Gamma_{\rm p}$ between measurement and simulation at $L_{\rm in} \sim L_{\rm out} \sim 3$ cm.

Analyzing these properties based on the particle balances, item 2) can be explained in term of the balance of $\Gamma_{\rm p} = \Gamma_{\rm g} - \Gamma_{\rm bf}$. As indicated by the simulations, they can be induced separately. A comparison of the IP and BP cases shows a decrease of the pumping flux fraction $\Gamma_{\rm p}/\Gamma_{\rm g}$ ($= 1 - \Gamma_{\rm bf}/\Gamma_{\rm g}$) by a factor of 0.7 in the BP case, indicating an increment of the back-flow flux $\Gamma_{\rm bf}$ through the two slots for BP. The fraction of $\Gamma_{\rm p}/\Gamma_{\rm g}$ is nearly constant, independent of the attached and detached conditions. Enhancement of the pumping efficiency under the detached MARFE condition in item 3) is caused by an increase of the incident flux fraction $\Gamma_{\rm g}/\Gamma_{\rm d}$ by a factor of 2~3 since the ionization front moves away from the divertor target and the fraction of ionized neutrals is significantly reduced. The item 1) in which the $\eta_{\rm p}$ depends on the divertor geometry will be discussed later in the next section.

Thus, the simulations for divertor pumping in the JT-60 U substantially reproduce the experimental results and provide a means to understand the pumping characteristics. Based on these results, control of the particles by divertor pumping is investigated in the next section, which focuses on the design study of the NCT divertor.

3.3 Particle controllability by divertor pumping in the NCT

In order to optimize the divertor design in the NCT (National Centralized Tokamak) where the heat and particle flux density in the divertor are considerably higher than those in the JT-60U, the heat load on the divertor targets, pumping capability, and geometric effect have been investigated using the SOLDOR/NEUT2D code [10].

A semi-closed divertor with the vertical target at an incidence angle of 45° with respect to the poloidal flux surface was proposed as part of the first conceptual design of the NCT. Cryopanels for inner and outer divertor pumping ($S_{\rm pump} \leq 200\,{\rm m}^3/{\rm s}$ each) are positioned under the private dome and outer divertor target, separately, based on the simulation results in Sec. 3.2; higher pumping efficiency is obtained by use of one exhaust slot in each pumping system such as that of the IP case.

Here, we evaluate the effects of the width of exhaust

slot (d_{in}, d_{out}) and the strike point position (L_{in}, L_{out}) in Fig. 12 (a) on divertor pumping since divertor pumping becomes a crucial issue for particle control under the high recycling conditions expected in NCT operation. For the simulation, Q_{total} is fixed to 12 MW (80% of input power at steady-state operation) and $\Gamma_{ion} = 1 \times 10^{22}$ s^{-1} is used, since this particle flux can be anticipated in the high recycling condition in JT-60U-size devices. Such high recycling condition is feasible by gas puffing or pellet injection. The fraction of carbon impurity to ion density is assumed to be 1%. A parameter survey is carried out regarding the slot widths of three cases and the strike positions of four cases, taking advantage of our code, i.e., its speedy calculation and flexibility.

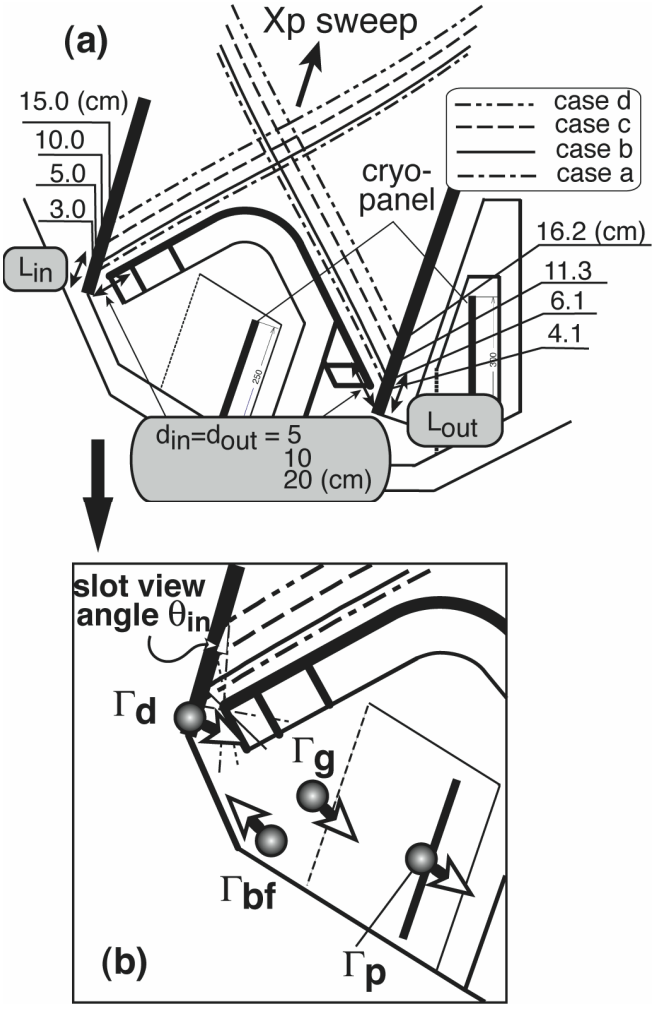

Fig. 12 (a) Schematic view of the NCT divertor when (d_{in}, d_{out}) and (L_{in}, L_{out}) are changed to evaluate the dependences of pumping efficiency on them. (d_{in}, d_{out}) are the width of exhaust slot between the private dome wing and the inner or outer divertor target, and changed by extending the dome wing. (L_{in}, L_{out}) are the distance from the dome wing extension point on the target to the strike point of separatrix similar to previous JT-60U analyses, and changed by sweeping the X-point. (b) Definition of the slot view angle θ_{in}. Neutral fluxes (Γ_d, Γ_g, Γ_{bf} and Γ_p) are defined in the same manner as those in Fig. 10.

The effect of the exhaust slot width (d_{in}, d_{out}) is evaluated in cases of 20, 10, and 5 cm. The strike point position is fixed to L_{in} = 3 cm and L_{out} = 4.1 cm. The pumping speed is fixed at 100 m^3/s on each cryopanel. The pumping efficiency is increased by narrowing the slot as shown in the hatched regions of Fig. 13. These features are also clarified by analyzing the neutral flux at the positions of the divertor target, exhaust slot, and cryopanel as shown in Fig. 12 (b), in a way similar to the previous JT-60U analyses. The generated flux of neutrals Γ_d originates mainly around the strike point on the divertor target with velocity in a nearly perpendicular direction in relation to the divertor target, with the main parts of those neutrals passing through the slot due to the vertical inclination of the divertor target. In such a condition, the back-flow fraction Γ_{bf}/Γ_g is reduced from 0.9 in the case of 20 cm in width to 0.8 in the case of 5 cm in width, while the pumping flux is increased. Consequently, the pumping efficiency ($\eta_p \equiv \Gamma_p/\Gamma_d$) for the 5 cm case is enlarged at a factor of ~3 in comparison with the 20 cm case.

The effect of strike point position is evaluated by changing the (L_{in}, L_{out}) in cases of $a \sim d$ as shown in Fig. 12 (a). Figure 13 shows the dependence of the pumping efficiency on the (L_{in}, L_{out}) in three cases of (d_{in}, d_{out}). The maximum pumping efficiency is obtained at a narrow width of $d_{in} = d_{out}$ = 5 cm at a position near the private dome (L_{in} = 3 cm, L_{out} = 4.1 cm) as mentioned above. However, it decreases steeply with an increase of L_{in} and L_{out}. This is led by a reduction of the incident fraction Γ_g/Γ_d with a decrease in the slot view angle θ_{in} as seen in Fig. 12 (b). As the slot width is increased, this dependent relationship is weakened by the balance between an increase of the back-flow fraction Γ_{bf}/Γ_g and an increase of Γ_g/Γ_d with larger θ_{in}. Typically, η_p at a slot width of 20 cm does not depend on the L_{in} and L_{out}, however, effi-

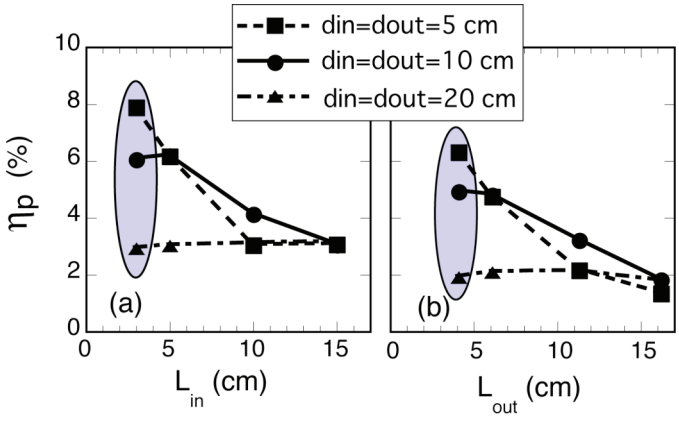

Fig. 13 Dependence of the distance from the strike point of separatrix to the dome wing extension point on inner (a) or outer (b) target on the pumping efficiency (η_p) in three cases of (d_{in}, d_{out}). S_{pump} = 100 m^3/s.

ciency is lowest in three cases due to a large Γ_{bf}/Γ_g. Relatively higher efficiency in wide regions of L_{in} and L_{out} is sustained at a slot width $d_{in} = d_{out} = 10$ cm.

These results indicate that the pumping efficiency is determined by balances of the incident and back-flow fluxes, depending on the divertor geometry and operational conditions. Further optimization of those two factors will be pursued in consideration of particle controllability and the flexibility of plasma shaping.

4. Summary

Integration of the SOL/divertor simulation codes of SOLDOR, NEUT2D, IMPMC and PARASOL is being developed by the JAEA for interpretation and prediction studies of SOL/divertor plasmas. Through the development of this code system, we aim to verify the physics models used in the fluid code on the basis of the PARASOL simulation. The physical processes of neutrals and impurities are treated by the Monte Carlo (MC) code to accomplish highly accurate simulations. The combined code with SOLDOR and NEUT2D has the following features: 1) a high-resolution oscillation-free scheme, TVD, applied using the finite-difference method of fluid equations, 2) neutral transport calculation under the complex divertor configurations including the pumping chamber with fine meshes (≤ 2 mm) near the divertor targets, 3) successful reduction of MC noise, and 4) optimization of MC calculation using the massive parallel computer. As a result, our code can obtain a steady state solution within $3 \sim 4$ hours, performing an effective parameter survey.

A simulation of the detached plasmas of the JT-60U reproduces the X-point MARFE well. It shows that the peaked radiation near the X-point is induced by the deep penetration of carbon impurities generated by chemical sputtering. The performance of divertor pumping in the JT-60U is evaluated based on particle balances. Cases of inside pumping (IP) and both-sides pumping (BP) for the attached/detached plasmas are investigated. Their performance can be characterized by the pumping efficiency $\eta_p[\equiv (\Gamma_p$; pumping flux)/$(\Gamma_d$; generated neutral flux at the target)]. We find that the degradation of η_p in the BP case is due to the increase of back-flow flux through the two exhaust slots. For NCT divertor design, the dependence of η_p on the width of the exhaust slot and the strike point position is studied. The maximum η_p can be obtained using a narrow slot of 5 cm among the 3 studied cases of 5, 10 and 20 cm at strike point positions of $L_{in} = 3$ cm and $L_{out} = 4.1$ cm. This is achieved by a significant reduction of the back-flow flux from the exhaust chamber. Leaving away the strike point from the exhaust slots, the η_p is decreased by the reduction of incident flux. Further optimization of geometry and operational conditions are the subjects of future research, taking particle controllability and the flexibility of plasma shaping into consideration.

The SOL/divertor codes developed by the JAEA are useful for interpreting the experimental results of the JT-60U as well as providing guidelines for future NCT divertor design.

Acknowledgements

The authors are grateful to the members of the JT-60 team and the NCT facility design team for their support and useful advice. They wish acknowledge Drs. H. Ninomiya, M. Kuriyama, M. Kikuchi, and N. Hosogane for their encouragement. This work is partly supported by a Grant-in-Aid for Scientific Research of Japan Society for the Promotion of Science.

Appendix. Piling Method

To reduce the Monte-Carlo (MC) noise, we carry out a number of MC calculations, averaging the results of scoring variables. When M sets of results are averaged, the noise is generally reduced by a factor of $1/\sqrt{M}$. The typical value of M is $15 \sim 100$ in our simulations. The memory size of scoring variables becomes huge, roughly $\sim$ (8 byte)

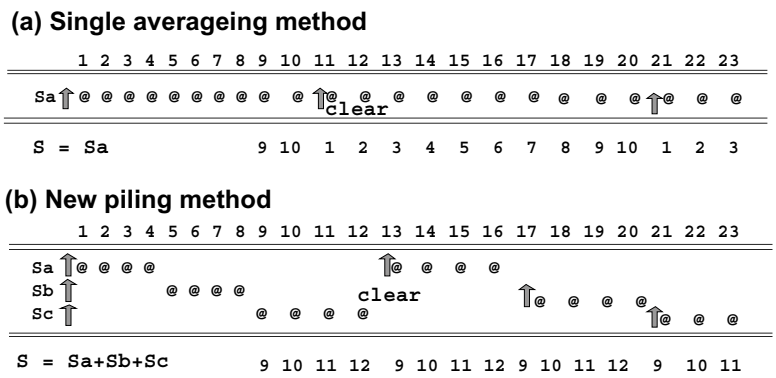

Fig. A1 Averaging methods of Monte-Carlo results. The sequential numbers denote the Monte-Carlo calculation cycle and the symbol (@) denotes the variable stored for the Monte-Carlo calculation at each time step. Each scoring variable is cleared at the timing indicated by an arrow. The variation of total scoring (S) in piling method is much smaller than that in the single averaging method.

$\times$ (M sets) $\times$ (6 sources) $\times$ (10^4 meshes) $\times$ (10 variables).

To reduce this large memory size, we introduced a piling method, which requires only three sets of scoring variables. The three sets (*Sa*, *Sb*, *Sc*) are provided and the latest calculation result is stored in a set selected from among *Sa*, *Sb*, and *Sc* as shown in Fig. A1 (b). This figure shows an example of the case of $M = 12$ groups. The scoring variables are cleared in some time sequence denoted by arrows. Source terms in the SOLDOR code are calculated using the total scoring $S = Sa + Sb + Sc$. In this procedure, they are averaged from the last 9 ($= 2(M/3) + 1$) groups to the last 12 ($= 3(M/3)$) groups. In the averaging method with a single set of scoring variables (Fig. A1 (a)), the reduction factor of the MC noise significantly changes from 1 to $1/\sqrt{M}$. In contrast, the factor in the piling method is flattened, i.e., $1/\sqrt{2(M/3)+1} \sim 1/\sqrt{M}$. This property in MC calculation using the piling method improves the convergence to a steady state.

[1] G. Janeschitz *et al*., J. Nucl. Mater. **290-293**, 1 (2001).
[2] R. Schneider *et al*., J. Nucl. Mater. **196-198,** 810 (1992).
[3] T.D. Rognlien *et al*., J. Nucl. Mater. **196-198,** 347 (1992).
[4] R. Simonini *et al*., J. Nucl. Mater. **196-198,** 369 (1992).
[5] K. Shimizu *et al*., J. Nucl. Mater. **313-316,** 1277 (2003).
[6] K. Shimizu *et al*., J. Nucl. Mater. **220-222,** 410 (1995).
[7] T. Takizuka, M. Hosokawa and K. Shimizu, Trans. Fusion Tech. **39,** 111 (2001).
[8] S. Ide and the JT-60 team, Nucl. Fusion **45**, S48 (2005).
[9] A. Isayama and the JT-60 team, Phys. Plasmas **12,** 056117 (2005).
[10] H. Kawashima *et al*., Fusion Eng. Des. **81**, 1613 (2006).
[11] H. Tamai *et al*., *Proc. 20th IAEA Fusion Energy Conf.* (Vilamoura, 2004) FT/P7-8, and references therein.
[12] B. Braams, A multi-fluid code for simulation of the edge plasma in tokamaks, NET rep. EUR-FU IXII-80-87-68, Comm. of the European Communities (1987).
[13] S.R. Chacravarthy and S. Osher, A new class of high accuracy TVD schemes for hyperbolic conservation laws, AIAA paper 85-0363 (1985).
[14] D.E. Post, J. Nucl. Mater. **220-222,** 143 (1995).
[15] M. Hughes and D. Post, J. Comput. Phys. **28,** 43 (1978).
[16] D.B. Heifetz *et al*., J. Comp. Phys. **46**, 309 (1982); D.B. Heifetz, *Physics of Plasma-Wall Interactions in Controlled Fusion* (D.E.Post and R.Behrisch, Eds., Plenum Press, New York and London, 1986) p.695.
[17] P.C. Stangeby and J.D. Elder, J. Nucl. Mater. **196-198,** 258 (1992).
[18] K. Shimizu *et al*., J. Nucl. Mater. **196-198,** 476 (1992).
[19] K. Shimizu *et al*., J. Nucl. Mater. **241-243,** 167 (1997).
[20] D. Reiser *et al*., Nucl. Fusion **38,** 165 (1998).
[21] K. Shimizu and T. Takizuka, *Proc. 27th EPS on Controlled Fusion and Plasma Physics*, (Budapest, Hungary), P4. 094 (2000).
[22] A.B. Ehrhardt and W.D. Langer, Princeton Plasma Physics Laboratory Report, PPPL-2477 (1987).
[23] K. Shimizu *et al*., Plasma Physics and Controlled Nuclear Fusion Research 1994 (Proc. 15th Int. Conf. Seville, 1994), Vol.**3**, IAEA, Vienna, 431 (1996).
[24] K. Shimizu and T. Takizuka, J. Plasma Fusion Res. **71,** 801 (1995).
[25] J. Roth *et al*., Atomic and Plasma-Material Interaction Data for Fusion (Supplement to the journal Nuclear Fusion) Vol. **1**, 63 (1991); J.V. Philips *et al*., J. Nucl. Mater. **313-316,** 354 (2003).
[26] S. Higashijima *et al*., J. Nucl. Mater. **266-269,** 1078 (1999).
[27] K. Shimizu and T. Takizuka, "Impurity transport code based on Monte Carlo techniques (IMPMC) ", Tech. Mtg on ITER Divertor Physics Design, Garching, 1994.
[28] P.C. Stangeby and J.D. Elder, Nucl. Fusion **35**, 1391 (1995).
[29] K. Shimizu *et al*., *submitted to* J. Nucl. Mater.
[30] R. Chodura, Phys. Fluids **25,** 1628 (1982).
[31] T. Takizuka and M. Hosokawa, Contrib. Plasma. Phys. **40,** 471 (2000).
[32] T. Takizuka, M. Hosokawa and K. Shimizu, J. Nucl. Mater. **313-316,** 1331 (2003).
[33] T. Takizuka and H. Abe, J. Comput. Phys. **25,** 205 (1977).
[34] A. Bergmann, Nucl. Fusion **42**, 1162 (2002).
[35] T. Takizuka and M. Hosokawa, *to be published in* Contrib. Plasma Phys. (2006).
[36] ITER Physics Basis, Nucl. Fusion **39,** 2391 (1999).
[37] T. Nakano, *Proc*. 4th *Fusion Energy Association Meeting of AESJ and JSPF*, 1A032 (2002).
[38] T. Fujimoto, Plasma Spectroscopy, ch.4 (Clarendon Press Oxford, 2004).
[39] S. Konoshima *et al*., J. Nucl. Mater. **313-316,** 888 (2003).
[40] H. Takenaga *et al*., Nucl. Fusion **41**, 1777 (2001).